Quasi-linear Kane conduction band model in nitrogen-doped indium tin oxide

Martin Markwitz,[1, 2, 3, *] Song Yi Back,[4] Edward X. M. Trewick,[1, 3] Peter P. Murmu,[2] Takao Mori,[4, 5] Ben J. Ruck,[1, 3] and John V. Kennedy[2, 3]

[1] *School of Chemical and Physical Sciences, Victoria University of Wellington, PO Box 600, Wellington 6140, New Zealand*
[2] *National Isotope Centre, GNS Science, PO Box 30368, Lower Hutt 5010, New Zealand*
[3] *The MacDiarmid Institute for Advanced Materials and Nanotechnology,*
Victoria University of Wellington, PO Box 600, Wellington 6140, New Zealand
[4] *International Center for Materials Nanoarchitectonics (WPI-MANA),*
National Institute for Materials Science (NIMS), 1-1 Namiki, Tsukuba, Ibaraki 305-0044, Japan
[5] *Graduate School of Pure and Applied Science, University of Tsukuba,*
1-1-1 Tennodai, Tsukuba, Ibaraki 305–8671, Japan

(Dated: January 16, 2024)

The band non-parabolicity of tin-doped indium oxide (ITO) polycrystalline thin films is investigated with the quasi-linear Kane model through Seebeck and Hall effect measurements. We report Kane model non-parabolic band parameters of $m_0^* = 0.21\,\mathrm{m_0}$ and $C = 0.52\,\mathrm{eV^{-1}}$ for ITO, in good agreement with historical photoemission, optical, and transport measurements. To do this, the ITO films were doped with nitrogen by ion implantation, with fluences ranging from $5 \times 10^{14}\,\mathrm{N\,cm^{-2}}$ to $5 \times 10^{15}\,\mathrm{N\,cm^{-2}}$. The presence of the nitrogen in the films was verified with X-ray photoelectron spectroscopy, and their acceptor character studied theoretically by density functional theory. Experimentally, the doped nitrogen formed $\mathrm{N_O}^-$ defects, deep acceptor states that led to a controlled compensation in carrier concentration from $10.1\times10^{20}\pm0.6\times10^{20}\,\mathrm{cm^{-3}}$ to $2.9\times10^{20}\pm0.2\times10^{20}\,\mathrm{cm^{-3}}$. Understanding the band non-parabolicity of degenerately doped transparent conducting oxides is essential for their commercial application in solar cells, transparent thermoelectric generators, and transparent thin film transistors, and by this work, the Seebeck and Hall effect approach with the quasi-linear Kane model for band non-parabolicity is presented as a practical method by which to study the variation in carrier effective mass without reliance on optical measurements.

I. INTRODUCTION

Band non-parabolicity is an important aspect of degenerately doped conducting oxides which leads to a limitation in the carrier mobility due to an increase in carrier effective mass as a function of carrier concentration. When the Fermi energy intersects an electronic band, high carrier concentrations are provided which leads to degenerate conductivity. A common class of degenerately doped conductors is the series of doped transparent conducting oxides, i.e., In_2O_3:Sn, In_2O_3:Mo, SnO_2:F, ZnO:Al, and ZnO:Ga, amongst others [1, 2]. In terms of industrial application, tin-doped In_2O_3 (ITO) is the current leading n-type transparent conducting oxide, found in transparent flat-panel screens and solar cells [3–5]. The key feature of the precursor In_2O_3 is its intrinsic band degeneracy from high concentrations of unintentional doping by oxygen vacancy (V_O) formation during growth. Tin doping by indium substitutional defect formation ($\mathrm{Sn_{In}}$) further n-type dopes In_2O_3, increasing its already high carrier concentration ($\sim 10^{21}\,\mathrm{cm^{-3}}$) and providing a Burstein-Moss blue shift without detrimentally affecting the materials' optical transparency ($> 80\,\%$) [5, 6]. The conduction band of In_2O_3 is composed of highly-disperse *s* orbitals which provides ITO with high carrier mobility ($\sim 50\,\mathrm{cm^2V^{-1}s^{-1}}$), and as a result a low electrical resistivity ($\sim 100\,\mathrm{\mu\Omega cm}$). The reason for high carrier mobility in In_2O_3 is the low carrier effective mass. Measurements of the effective mass have predicted a wide range of possible values, ranging between $0.14\,\mathrm{m_0}$ and $0.55\,\mathrm{m_0}$ reported through a range of methods, where $\mathrm{m_0}$ is the free electron rest mass [5–10]. A recent Seebeck and Hall effect measurement approach in ITO found an effective mass of $0.30 \pm 0.03\,\mathrm{m_0}$ [11]. From band edge absorption measurements, reduced masses of $0.38\,\mathrm{m_0}$ and $0.22\,\mathrm{m_0}$ were calculated both without and with many-body correction terms for the Burstein-Moss band gap shift correction [12]. Density functional theory (DFT) calculations from Fuchs *et al.* [9] find band-edge effective masses of $0.18\,\mathrm{m_0}$ by the PBE exchange-correlation functional and $0.22\,\mathrm{m_0}$ by the HSE03 exchange-correlation functional.

A limiting factor in carrier mobility, and by extension, electrical conductivity in ITO is the increase in effective mass due to conduction band non-parabolicity. The band edge effective mass is denoted m_0^* and the first-order non-parabolicity factor is C. The effective mass variation as a function of carrier concentration in ITO has been investigated so far only through optical methods involving the plasma frequency, Liu *et al.* [4], Fujiwara and Kondo [13], and Feneberg *et al.* [14], finding near band edge effective masses of $m_0^* = 0.263\,\mathrm{m_0}$, $m_0^* = 0.297\,\mathrm{m_0}$ and $m_0^* = 0.18\,\mathrm{m_0}$, with first-order non-parabolicity factors of $C = 0.4191\,\mathrm{eV^{-1}}$, $C = 0.18\,\mathrm{eV^{-1}}$ and $C = 0.5\,\mathrm{eV^{-1}}$, respectively. To our best knowledge, no investigation of the non-parabolicity of the conduction band in ITO through the Seebeck and Hall effect approach has yet been reported.

---

[*] m.markwitz@gns.cri.nz

The high carrier concentration in ITO is a result of both the oxygen vacancy defect and the tin donor defect, the former providing two free electrons and the latter one additional free electron [12]. The activity of the tin defect can be modified through crystallographic damage induction by ion implantation, an effect noted in polycrystalline and epitaxial films, but not in amorphous films [15]. A significant reduction in carrier mobility after implantation is also observed, suspected to be due to formation of point defects formed by the damage cascades, which involve both indium and tin oxides. Annealing under vacuum conditions between 200-300°C is known to remedy the loss in carrier mobility by reparation of those point defect structures [16]. The post-anneal carrier concentration is also known to recover to close to the carrier concentrations observed in the unimplanted film, attributed to the re-activation of the tin as an electron donor. It has been reported through this approach that tin doping indium oxide provides at most $\sim 4\times10^{20}\,\mathrm{cm^{-3}}$ electrons to indium oxide [12]. Excessive doping with tin leads to a notable reduction in carrier mobility due to an increase in scattering centers, whilst the additionally doped tin remains largely inactive.

Nitrogen implantation is a known extrinsic doping method in n-type transparent conducting oxides by which to effectively tune their structural, optical, and electrical properties through carrier compensation [17–19]. By using ion implantation we tune the carrier concentration in ITO by compensating its free carrier concentration with nitrogen as an acceptor dopant which substitutes onto oxygen sites (N_O). We implement the Seebeck and Hall effect measurement method on magnetron sputtered and nitrogen implanted ITO thin films to investigate of the non-parabolicity of the conduction band. The implanted nitrogen is observed to form N_O^- substitutional defects, acting as an acceptor in ITO. This method reduces the overall carrier concentration and allows for a fine-tuning of the Fermi energy relative to the conduction band edge in ITO, without causing any other complicating adverse effects in terms of film or material degradation. The measurements presented in this work show a controlled reduction in carrier concentration through nitrogen implantation. A theoretical investigation was also undertaken to investigate the role of the N_O defect with, and without nearby Sn_{In} defects, revealing a stable N_O^- defect regardless of the nearby Sn_{In} impurity concentration, whilst simultaneously not influencing the dispersion of the conduction band.

II. EXPERIMENTAL METHODS

ITO films (170−175 nm thick) were acquired from techinstro, possessing a 25 nm SiO_2 buffer layer on 0.7 mm borosilicate glass substrates. The ITO films were implanted with nitrogen at normal incidence over a range of fluences from $5\times10^{14}\,\mathrm{N\,cm^{-2}}$ to $5\times10^{15}\,\mathrm{N\,cm^{-2}}$. T-DYN (Transport of Ions in Matter-Dynamic) was used to identify an appropriate implantation energy of 57.6 keV, leading to a projected range of $R_p = 76.2\,\mathrm{nm}$ [20] with an assumed ITO density of $7.14\,\mathrm{gcm^{-3}}$. The fluences used for this work led to peak nitrogen concentrations between $0.06 - 0.6\,\%$ at R_p. The resulting nitrogen depth profile is depicted in supplemental information Figure S1. Experimentally, the implantation was conducted at room temperature with a low energy ion implanter with a 90° mass-separating magnet, the beam scanned to ensure uniform implantation over the entire film area [21–23]. The nitrogen beam current density was kept constant at $0.3\,\mathrm{\mu Acm^{-2}}$ to avoid sample heating. The base pressure in the target chamber was kept below 5×10^{-8} hPa throughout implantation. After implantation the samples were vacuum-annealed at 300°C for one hour at a pressure less than 2×10^{-6} hPa in a custom-built vacuum tube furnace.

Film thickness characterization was conducted with Rutherford Backscattering Spectrometry (RBS) with a 10 nA 2.0 MeV $^4He^+$ beam at normal incidence with a beam spot size of $1\,\mathrm{mm}^2$ for a total charge of 20 µC with the detector mounted at 165° relative to the incident beam [24]. The films' structural properties were investigated with X-ray diffraction (XRD) with a Cu K $\alpha_{1/2}$ X-ray source (K α_1 $\lambda = 1.540\,\text{Å}$, K α_2 $\lambda = 1.544\,\text{Å}$). The measurement geometry was grazing incidence with $\omega = 2°$ with a Rigaku SmartLab X-ray diffractometer. X-ray photoelectron spectroscopy (XPS) was used to investigate the chemical composition with a ThermoFisher ESCALAB250Xi using a monochromated Al K α_1 (1486.68 eV) X-ray source with perpendicular photoelectron emission. The largest C 1*s* peak was used for binding energy alignment for the high resolution scans at 284.8 eV, and an intrinsic binding energy error of 0.1 eV was assumed. The data was analysed with CasaXPS [25]. The pass energy used for measurement was 100 eV for the survey scans and 20 eV for the core level scans. The base pressure in the vacuum system was kept better then 2×10^{-9} hPa throughout measurement.

The room temperature electrical properties were measured on $10\times10\,\mathrm{mm}^2$ samples with a Hall effect measurement system (HMS-3000) with a 0.55 T magnet using gold contact electrodes pressed on the sample surfaces. Room temperature thermoelectric measurements were done with a ULVAC ZEM-3 Seebeck effect measurement system. The error in the electrical conductivity and Seebeck effect measurements are 5 %, respectively. Temperature dependent resistivity measurements were conducted with a custom-built closed-cycle cryostat with the Van der Pauw geometry.

III. COMPUTATIONAL METHODS

The *ab initio* density functional theory (DFT) calculations in this work were conducted with `Quantum ESPRESSO` using the periodic pseudopotential method within the projector augmented wave formalism [26–29]. Ultrasoft pseudopotentials by Dal Corso were used with the generalized-gradient approximation (GGA) level of theory with the PBE functional [30, 31]. The indium, tin, oxygen, and nitrogen valence atomic configurations were $4d^{10}5s^25p^1$, $4d^{10}5s^25p^2$, $2s^22p^4$, and $2s^22p^3$, respectively. Convergence testing was conducted on an 80 atom bixbyite unit cell of $\mathrm{In_2O_3}$ in the $\mathrm{Ia\bar{3}}$ (group no. 206) structure, containing 32 In atoms and 48 O atoms. The energy per atom and force convergence criteria were $< 5\,\mathrm{meV\,atom^{-1}}$ and $< 1\,\mathrm{meV\,Å^{-1}}$, respectively, and involve a $3 \times 3 \times 3$ Monkhorst-Pack k-point grid [32] with cutoff energy 67 Ry (912 eV). Gaussian smearing of 0.01 eV was used due to the induced metallicity by the defects. Symmetry-unrestricted structure optimization was conducted with the conjugate gradient algorithm by calculating the Hellman-Feynman forces. Due to the reduced Brillouin zone size of the supercell, the unfolded band structure was subsequently calculated with banduppy [33–35]. For the projected density of states calculations, a $12 \times 12 \times 12$ Monkhorst-Pack grid was used with 0.1 eV Gaussian broadening.

The effect of tin stoichiometry on the electrical behavior of the $\mathrm{N_O}$ acceptor defect is tested by considering an isolated $\mathrm{N_O}$ defect, a $\mathrm{N_O}$ defect with a nearby $\mathrm{Sn_{In}}$ defect, denoted ($\mathrm{Sn_{In}}$+$\mathrm{N_O}$), and a $\mathrm{N_O}$ defect with two nearby $\mathrm{Sn_{In}}$ defects (2$\mathrm{Sn_{In}}$+$\mathrm{N_O}$). The range of $\mathrm{N_O}$, ($\mathrm{Sn_{In}}$+$\mathrm{N_O}$), and (2$\mathrm{Sn_{In}}$+$\mathrm{N_O}$) defects are used to study nitrogen doping of $\mathrm{In_2O_3}$ and heavily Sn-doped $\mathrm{In_2O_3}$, where the concentration of $\mathrm{N_O}$ defects is lower than that of the $\mathrm{Sn_{In}}$ donors, without requiring intractably large supercell calculations. The various defect charge states and their formation energies determine the Fermi energy of a physical system. The formation energy of a defect (ΔH_D^q) depends on the charge state (q) and defect type (D) of the total energy of the defected supercell (E_D^q), its pristine host energy (E_H), the chemical potential(s) ($\mu_i + \Delta\mu_i$) of the subtracted/added atom(s) ($n_i = -1/+1$), the electron energy $q\Delta E_F$, and finite size correction factors by E_C in

$$\Delta H_D^q = [E_D^q - E_H] - \sum_i n_i\,(\mu_i + \Delta\mu_i) + q\Delta E_F + E_\mathrm{C}. \quad (1)$$

The thermodynamic host stability condition of the metal oxide formation enthalpy $\Delta H_f(\mathrm{In_2O_3}) = 2\Delta\mu_\mathrm{In} + 3\Delta\mu_\mathrm{O} = -9.49\,\mathrm{eV}$ is enforced. For the formation enthalpy of tin and indium their ambient metallic phases are considered whilst for nitrogen and oxygen the gaseous molecules are used. The formation enthalpy of tin is also limited through the formation of rutile $\mathrm{SnO_2}$. Important, also, is the thermodynamic transition energy which is the Fermi energy at which a defect changes charge from state q_1 to q_2, given by

$$\varepsilon(q_1/q_2) = \frac{\Delta H_D^{q_1}(\Delta E_F = 0) - \Delta H_D^{q_2}(\Delta E_F = 0)}{q_2 - q_1}. \quad (2)$$

This quantity determines if the defect is a deep, shallow, or resonant donor/acceptor within a host electronic structure, depending if the transition occurs far, near, or within a band edge. The defect formation energy correction factors used in this work are: (1) core level potential alignment to the furthest indium atom from the defect site, and (2) third order periodic image charge correction. For the image charge correction a relative permittivity of 8.9 [36] and the bcc supercell Madelung constant 2.8883 [37] were used with $f = -0.34$ [38]. From our calculation, the Kohn-Sham eigenvalue gap in pristine $\mathrm{In_2O_3}$ is underestimated to be 0.9 eV, much less than the experimental fundamental gap of 2.7 eV [39]. We correct the band gap by a valence band downshift ($\Delta E_\mathrm{VB} = -0.46\,\mathrm{eV}$) determined through a $U_\mathrm{eff} = U - J = 5.6\,\mathrm{eV}$ ($J = 0$) Hubbard parameter applied to the In $4d$ valence states correcting the O $2s$ depth shift relative to the valence band edge, and a conduction band upshift (ΔE_CB) by the scissor shift to correct the remaining discrepancy [40–43]. For the formation energy diagram the Fermi energy is allowed to vary between the shifted band edges $0 \leq \Delta E_F \leq E_G$.

IV. COMPUTATIONAL RESULTS

Ab initio density functional theory calculations were undertaken to explicate the role of the charge state of the $\mathrm{N_O}$ defect. The characteristic n-type defects in ITO which define its physical characteristics are intrinsic oxygen vacancies (V_O) and extrinsic tin-indium impurity defects ($\mathrm{Sn_{In}}$). Figure 1 shows the application of Eq. 1 in In-rich and O-rich chemical potentials. In Figure 1 the oxygen vacancy (black) exists in either the 2+ or the 0 charge state depending on the Fermi energy, transitioning at $\Delta E_F = 2.58\,\mathrm{eV}$ by Eq. 2. The $\varepsilon(2+/0)$ charge transition of V_O at 0.12 eV below the conduction band edge is close to the LDA-calculated value of 0.2 eV reported by Reunchan *et al.* [44] and the HSE-calculated value of 0.21 eV calculated by Yu *et al.* [45]. Chatratin *et al.* predicted two charged transitions: $\varepsilon(2+/+)$, and $\varepsilon(+/0)$ at 0.12 eV below, and 0.06 eV above the conduction band edge as calculated with the hybrid HSE functional [46]. Lany and Zunger [40] predicted a deeper $\varepsilon(2+/0)$ transition 2.3 eV above the valence band edge with PBE while assuming a band gap of 3.5 eV. Recently, Swallow *et al.* [47] predicted a transition at 0.12 eV below the conduction band edge with an assumed gap of 2.63 eV with HSE. A consensus of the V_O charge transition energy of is yet to be reached.

Including one $\mathrm{Sn_{In}}$ (orange) defect corresponds to a doping concentration of x=0.06 in $\mathrm{In_{2\text{-}x}Sn_xO_3}$. The preferred charge state of this defect is $\mathrm{Sn_{In}}^+$ when the Fermi level is near the gap centre with a transition to an inactive $\mathrm{Sn_{In}}^0$ state at $\Delta E_F = 2.35\,\mathrm{eV}$, 0.35 eV below the conduction band edge, and is therefore a deep donor in $\mathrm{In_2O_3}$. In the In-rich condition, the formation energy of the $\mathrm{Sn_{In}}$ defect is always negative, in violation of the dilute limit condition. This, however, qualitatively indicates that this extrinsic defect can be readily incorporated in the $\mathrm{In_2O_3}$. Lany and Zunger [40] predict with PBE that the

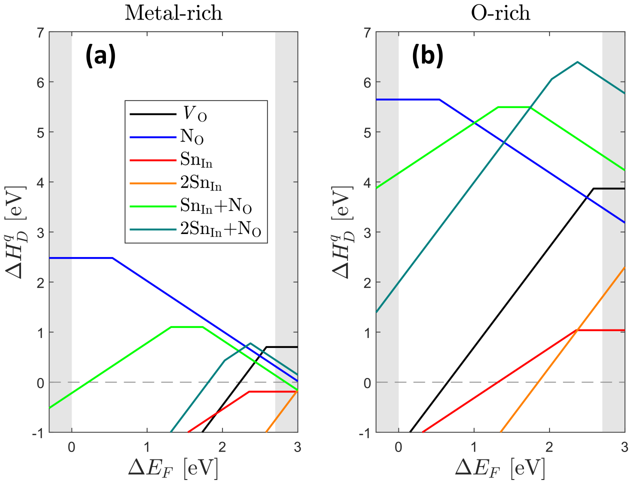

FIG. 1. (Color online) Formation energy diagram of defect states in the (a) In-rich scenario ($\Delta\mu_{\mathrm{In}} = 0\,\mathrm{eV}$) and the (b) O-rich scenario ($\Delta\mu_{\mathrm{O}} = 0\,\mathrm{eV}$). The background coloring indicates the in-band regions beyond the fundamental gap of 2.7 eV.

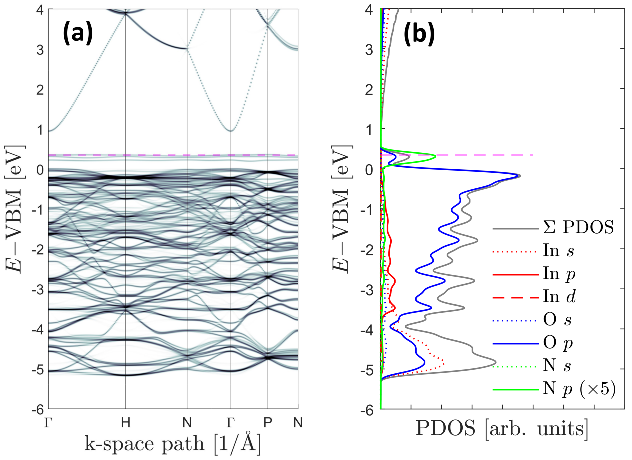

FIG. 2. (Color online) Near-edge (a) unfolded band structure and (b) projected density of states diagram of In_2O_3 unit cell possessing one neutral N_O defect. The energy scale is set relative to the valence band maximum, and the Fermi energy is depicted by the magenta dashed line. In the projected density of states the N p contribution has been multiplied by 5 to increase its visibility.

$\varepsilon(+/0)$ transition occurs 0.13 eV below the conduction band edge, acting in that case as a deep donor, while Swallow *et al.* [47] predict the $\varepsilon(+/0)$ transition to occur at 0.85 eV above the conduction band edge. When considering an increased tin concentration by including two $\mathrm{Sn_{In}}$ (red) defects the preferred charge states are $2\mathrm{Sn_{In}}^{2+}$ and $2\mathrm{Sn_{In}}^{0}$. The stable charge state directly transitions undergoes the $\varepsilon(2+/0)$ transition at $\Delta E_F = 3.08\,\mathrm{eV}$, 0.38 eV above the conduction band edge. This defect charge transition lies within the conduction band, and as such, would lead to degenerate doping of indium oxide. Including two $\mathrm{Sn_{In}}$ defects leads to an overall decreased defect stability, i.e., a higher formation energy per defect.

The nitrogen-oxygen substitution was then investigated in a variety of scenarios: the first involving just $\mathrm{N_O}$ (blue), the second involving a defect complex of $\mathrm{Sn_{In}}$+$\mathrm{N_O}$ (light green), and the third involving a defect complex of $2\mathrm{Sn_{In}}$+$\mathrm{N_O}$ (dark green). The $\mathrm{N_O}$ defect undergoes the $\varepsilon(0/-)$ transition at $\Delta E_F = 0.54\,\mathrm{eV}$, acting therefore as a deep acceptor in indium oxide. The deep acceptor status calculation of the $\mathrm{N_O}$ defect is a similar as noted in the other transition metal oxides such as ZnO [48, 49] and $SrTiO_3$ [44]. The nitrogen substitution directly compensates the intrinsic donor V_{O} defect by filling the oxygen vacancy. Considering the $\mathrm{Sn_{In}}$+$\mathrm{N_O}$ defect complex reveals a similar character, undergoing the $\varepsilon(+/0)$ transition at $\Delta E_F = 1.32\,\mathrm{eV}$ and the $\varepsilon(0/-)$ transition at $\Delta E_F = 1.74\,\mathrm{eV}$, accounting for both sub-transitions of $\mathrm{N_O}^0$ to $\mathrm{N_O}^-$ and $\mathrm{Sn_{In}}^+$ to $\mathrm{Sn_{In}}^0$. These transitions are located close to the middle of the experimental gap. Further, the $2\mathrm{Sn_{In}}$+$\mathrm{N_O}$ defect complex reveals a series of charge transitions, ranging from $(2\mathrm{Sn_{In}}+\mathrm{N_O})^{2+}$ to $(2\mathrm{Sn_{In}}+\mathrm{N_O})^{-}$ with thermodynamic transitions at $\Delta E_F = 2.03\,\mathrm{eV}$ for $\varepsilon(2+/+)$ and $\Delta E_F = 2.37\,\mathrm{eV}$ for $\varepsilon(+/-)$. All defects involving nitrogen exhibit persistent acceptor character when the Fermi energy lies near or within the conduction band. The nitrogen defect in ITO is predicted to monotonically reduce the experimentally observed free carrier concentration, regardless of the activity of presence of nearby tin donors.

The neutral $\mathrm{N_O}$ acceptor defect is investigated in more detail through an unfolded band structure diagram and projected density of states diagram in Figure 2(a) and Figure 2(b). The band structure shows the standard features of In_2O_3, a rather complicated valence band structure, and a single conduction band separated by a band gap. The conduction band centred at Γ exhibits obvious non-parabolicity when sufficiently far from the conduction band edge. The density of states diagram shows that the valence band is mainly comprised of states with O p and In p character and that the conduction band is comprised of a dispersive band of In s states. The $\mathrm{N_O}$ defect reveals a localized N defect state (delocalized in reciprocal space) near to the valence band maximum. Note that in the absence of other defects this would pin the Fermi level to the $\mathrm{N_O}$ defect energy. The $\mathrm{N_O}$ defect does not perturb the dispersion of the conduction band. The lack of disturbance of the conduction band is attributed to the absence of significant indium sublattice distortion upon force and pressure relaxation. Figure 3 shows the electron density difference diagram of the $\mathrm{N_O}^-$-$\mathrm{N_O}^0$ electron density, visualized with VESTA [50, 51]. The electronic defect state is localized to the $\mathrm{N_O}$ defect site.

In terms of the cell structure, for the cell containing one $\mathrm{N_O}^{-1}$ defect the average nearest-neighbor N-In distance is 2.174 Å. Comparing this to the same site in the defect-free unit cell the average nearest-neighbor O-In distance

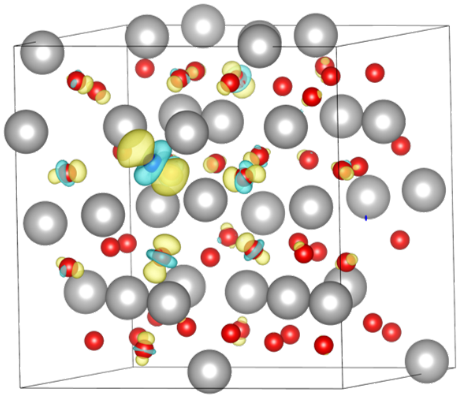

FIG. 3. (Color online) Electron density difference diagram of the 80-atom bixbyite unit cell of In_2O_3 with one N_O defect. Red spheres are oxygen atoms, grey spheres are indium atoms, and the blue sphere is a nitrogen atom. The yellow and blue colored regions are positive and negative electron density differences.

is 2.178 Å, a negligible difference compared to the N-In distance. The equilibrium lattice constant of the defected supercell with one N_O^- defect is 10.365 Å whilst for the pristine system it is 10.303 Å, a difference of less than 0.5 %. The localization of the N_O p states above the valence band are highlighted in the projected density of states in Figure 2(b). Importantly there is no change of the electron density localized on the metal ions. The absence of lattice distortion and negligible effect on the electron density around the overlapping free electron-like In s orbitals implies that the overall conduction behavior is minimally affected by the presence of N_O^- defects. In summary, this section verifies that nitrogen doping ITO leads to carrier compensation without introducing disorder within the conduction band. The next section provides experimental evidence of N_O defect formation through combined variation in carrier concentration and carrier mobility.

V. EXPERIMENTAL RESULTS

Through RBS measurement, the film stoichiometry was identified to be approximately 2:3 metal to oxygen with a film thickness of 173 ± 2 nm, data shown in supplemental information Figure S2(a). From XRD measurements shown in supplemental information Figure S2(b), phase-pure In_2O_3 (card no. 00-006-0416) was identified, with high film crystallinity for all samples. Split pseudo-Voigt functions were fitted to the three dominant diffraction peaks in the pattern, after which the lattice constant was calculated with Bragg's law, then averaged over the three most intense diffractions to estimate the lattice constant [52]. No measurable changes in lattice constant or peak broadness were observed after implantation, staying within error of the 10.18 ± 0.01 Å lattice constant of the unimplanted sample.

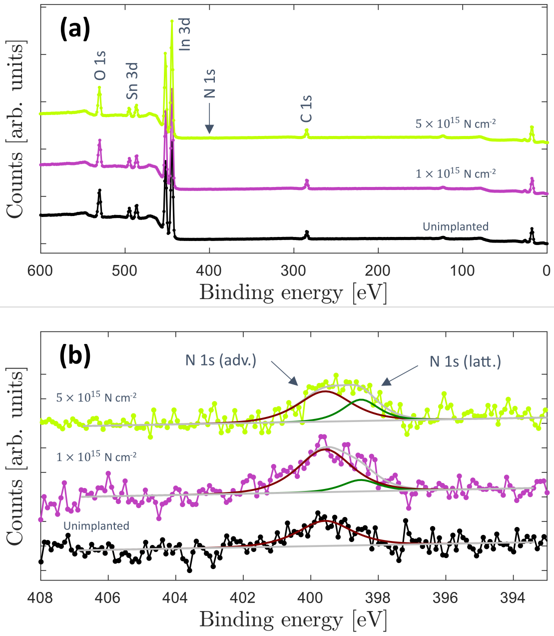

FIG. 4. (Color online) XPS (a) survey scans, and (b) high resolution N 1s core level scans of undoped and nitrogen doped ITO films with annotated peak fits. Data is vertically offset for visual clarity.

To identify the ratio of tin to indium and to verify the presence of nitrogen in the films, a selection thereof were investigated with XPS. Figure 4(a) shows the survey spectra of films which indicating the presence of carbon, indium, tin, and oxygen. High resolution XPS was conducted on the C 1s, N 1s, In 3d, Sn 3d, and O 1s core levels. The N 1s core level is shown in Figure 4(b), whilst the In 3d, Sn 3d, C 1s, and O 1s core levels are shown in Figure 5.

Figure 5(a) shows the indium core levels which can be fitted into two sets of two peaks at 444.3 eV for lattice indium in ITO, designated In $3d_{5/2}$ (latt.), and at 445.2 eV corresponds to amorphized In in ITO, denoted as In $3d_{5/2}$ (amorph.) [53, 54]. The corresponding In $3d_{3/2}$ peaks are spin-orbit separated by 7.54 eV. Figure 5(b) shows the Sn 3d core level, separated into two sets of two peaks, the first at 486.2 eV, attributed commonly to Sn $3d_{5/2}$ (2+) and the second at 486.8 eV as Sn $3d_{5/2}$ (4+). The Sn 4+ peak represents the presence of both substitutional Sn_{In} doping and the presence of SnO_2, making their presence indistinguishable [55, 56]. In addition, it is known that tin oxides form at the boundaries between In_2O_3 grains due to the expulsion of Sn during growth of ITO films. The corresponding Sn $3d_{3/2}$ peaks are spin-orbit separated by 8.41 eV. The fits for the O 1s peaks in Figure 5(c) at 530.0 eV are attributed to lattice oxygen denoted as O 1s (latt.) in In_2O_3, with the peaks around 1 eV binding energies above at 531.2 eV are commonly interpreted as oxygen in the proximity of an oxygen-deficient indium atom, denoted as O 1s (vac.) [55, 57, 58]. Oxy-

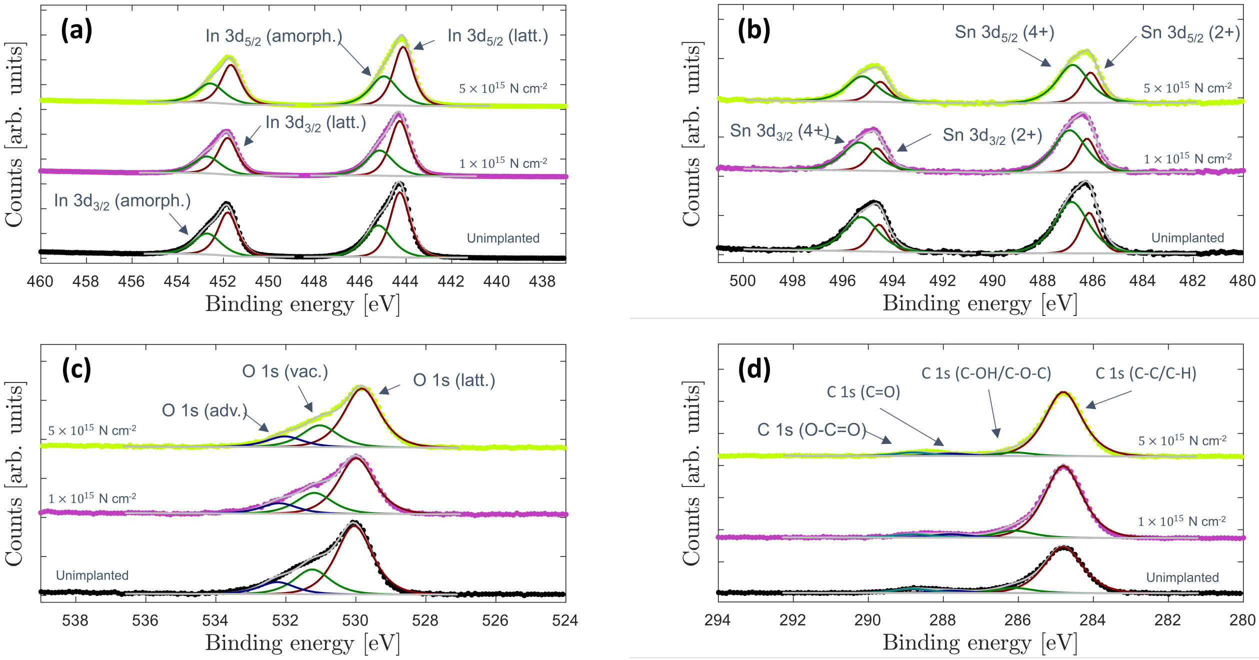

FIG. 5. (Color online) XPS high resolution (a) In 3d, (b) Sn 3d, (c) O 1s, and (d) C 1s core level scans of undoped and nitrogen doped ITO films with annotated peak fits. Data is vertically offset for visual clarity.

gen core levels associated with adventitious hydrocarbons are noted as O $1s$ (adv.) at 532.2 eV. The fits in the C $1s$ core level in 5d at 284.8 eV (C-C/C-H), 286.1 eV (C-OH/C-O-C), 287.8 eV (C=O), and 288.8 eV (O-C=O) were assigned as by Biesinger [59].

Nitrogen core level spectra are shown in Figure 4(b) where it is noted that all samples show a small concentration of nitrogen at a binding energy of 399.6 eV, attributed to the presence of adventitious hydrocarbons by atmospheric exposure [60–62]. The intensity of the adventitious N $1s$ peak scales directly with intensity of the adventitious carbon-related peaks, indicating their origin. The implanted samples show a peak at 398.5 eV which has been previously attributed to nitrogen on oxygen substitution within ITO [55, 63]. The implanted nitrogen ions are proposed to either fill oxygen vacancies or substitute oxygen atoms, and therefore form deep acceptor states, having the effect of reducing the overall carrier concentration. After Ar^+ sputter etching for two minutes the bulk tin-indium ratio was identified to be 0.08:0.92, resulting in a film stoichiometry of $In_{1.84}Sn_{0.16}O_3$. The chemical species associated with adventitious hydrocarbons (not shown) on the film surface were almost entirely removed (C, N, and O) after etching. Simultaneously, the nitrogen core level became hidden within the measurement noise due to preferential sputtering [64].

The atomic concentration of nitrogen at the projected range depending on the implantation fluence by T-DYN is shown in Table I. A continuous decrease in conductivity by implantation was observed as a result of nitrogen doping. Since the films are degenerately donor-doped semiconductors, no minority carriers are formed by the introduction of the deep acceptor states, and therefore, the Hall coefficient is derived from a single-carrier model. From the measured Hall coefficient R_H, the carrier concentration n was calculated through $n = 1/qR_H$. The Hall coefficient was negative in all samples, implying that the films remain n-type conductors. The carrier mobility is defined in terms of the electrical conductivity and carrier concentration as $\mu = \sigma/nq$. Upon implantation with the lowest fluence ($5 \times 10^{14}\,\mathrm{N\,cm^{-2}}$), a notable initial decrease in carrier concentration and mobility from an initial $9.5 \times 10^{20} \pm 0.6 \times 10^{20}\,\mathrm{cm^{-3}}$ and $43.1 \pm 4.5\,\mathrm{cm^2V^{-1}s^{-1}}$ to values of $5.5 \times 10^{20} \pm 0.3 \times 10^{20}\,\mathrm{cm^{-3}}$ and $22.1 \pm 2.3\,\mathrm{cm^2V^{-1}s^{-1}}$ were measured. The initial reduction of both has been previously attributed to the formation of neutral tin and indium defect complexes [10, 12, 65]. Beyond this initial drop in mobility, the mobility only slightly further reduced upon further implantation which is attributed to the increasing concentration of nitrogen impurity sites. A final carrier mobility value of $17.1 \pm 1.8\,\mathrm{cm^2V^{-1}s^{-1}}$ was measured upon implantation with a fluence of $5 \times 10^{15}\,\mathrm{N\,cm^{-2}}$. The further reduction in carrier concentration is directly proportional to the implanted nitrogen concentration, implying that the nitrogen doping acts exclusively as an acceptor. The initial significant reduction in carrier concentration is attributed to the deactivation of the tin donor, removing an average $3.9 \times 10^{20} \pm 0.2 \times 10^{20}\,\mathrm{cm^{-3}}$ carriers in all un-annealed samples. This result is in close agreement with the donor concentration derived from the tin donors as calculated by Vink *et al.* [12]. This relationship between implanted

TABLE I. Room temperature electrical and thermoelectric properties of both implanted and un-annealed, and implanted and annealed nitrogen doped indium tin oxide thin films.

Fluence [N cm^{-2}]	N conc. [$\times 10^{20}$ cm^{-3}]	Annealed	ρ [µΩcm]	σ [Scm^{-1}]	μ [cm^{2}V^{-1}s^{-1}]	$\lvert n \rvert$ [$\times 10^{20}$ cm^{-3}]	$\lvert \alpha \rvert$ [µVK^{-1}]
0	0	×	156 ± 8	6427 ± 323	42.5 ± 4.3	9.5 ± 0.6	11.5 ± 0.6
5×10^{14}	0.3	×	514 ± 26	1945 ± 97	22.1 ± 2.3	5.5 ± 0.3	12.7 ± 0.7
1×10^{15}	0.6	×	685 ± 34	1460 ± 73	19.2 ± 2.0	4.8 ± 0.3	15.6 ± 0.8
2.5×10^{15}	1.5	×	814 ± 47	1229 ± 70	19.0 ± 2.0	4.0 ± 0.3	17.1 ± 0.9
5×10^{15}	2.9	×	1259 ± 67	794 ± 42	17.1 ± 1.8	2.9 ± 0.2	18.8 ± 1.0
0	0	✓	143 ± 7	6993 ± 352	43.1 ± 4.5	10.1 ± 0.6	10.0 ± 0.5
5×10^{14}	0.3	✓	180 ± 9	5547 ± 278	38.9 ± 4.0	8.9 ± 0.5	11.5 ± 0.6
1×10^{15}	0.6	✓	198 ± 10	5060 ± 254	38.3 ± 3.9	8.2 ± 0.4	11.7 ± 0.6
2.5×10^{15}	1.5	✓	246 ± 12	4065 ± 204	39.7 ± 4.2	6.4 ± 0.4	13.4 ± 0.7
5×10^{15}	2.9	✓	373 ± 19	2684 ± 134	38.2 ± 3.9	4.4 ± 0.2	17.9 ± 0.9

nitrogen fluence and the variation in carrier concentration is visualized in supplemental information Figure S3. Interestingly, from XPS, the overall tin concentration was measured to be $2.1 \pm 0.1 \times 10^{21}$ cm^{-3}, implying that the overall doping efficiency of tin is only 16.1 ± 0.8 %. This implies that the majority of tin in ITO is likely located at boundaries between crystal grains of tin-doped In_2O_3.

The sign of the Seebeck coefficient was negative in all samples implying that the films are n-type conductors. The magnitude of the Seebeck coefficient increased continuously from -11.5 ± 0.6 µVK^{-1} for the unimplanted film to -18.8 ± 1.0 µVK^{-1} for the film implanted with 5×10^{15} N cm^{-2}. A similar trend of increasing magnitude of the Seebeck coefficient is noted in the annealed samples, ranging from -10.0 ± 0.5 µVK^{-1} to -17.9 ± 0.9 µVK^{-1}. The Seebeck coefficient and carrier concentration are related to one-another through the density of states, of which the energy dependence directly depends on the carrier effective mass and band non-parabolicity. The relationship between the two properties can be visualized by plotting the Seebeck coefficient and carrier concentration, where an increase in one leads to a monotonic decrease in the other.

To repair the point defects induced by implantation the samples were annealed under vacuum. Vacuum annealing led to a dramatic increase in carrier mobility, close to the mobility of the unimplanted sample, summarized in Table I. Through annealing the carrier concentration and therefore electrial conductivity also increased, attributed to the reactivation of the tin donors.

In order to quantify the relationship between the carrier concentration and Seebeck coefficient, the scattering parameter must be known. The scattering parameter is a constant which relates the energy of a carrier to its lifetime, defined in the Boltzmann transport formalism in the power law relaxation time by

$$\tau(E) = \tau_0 \left(E/k_B T\right)^r \tag{3}$$

where τ_0 is the scattering time constant, E the carrier energy (relative to the conduction band edge), k_B is Boltzmann's constant, T is the absolute temperature, and r is the scattering parameter, relating carrier energies and lifetimes. Different scattering mechanisms possess different scattering factors, which also relates to the temperature dependence of that scattering mechanism, the ones relevant to this work being neutral impurity scattering with $r = 0$ and deformation potential scattering with $r = -0.5$ [52]. The scattering parameter near room temperature can be inferred from temperature dependent mobility measurements. In the case of ITO, the temperature dependence of the resistivity also reveals the scattering mechanism since the temperature dependence of the carrier concentration is negligible due to its degenerate doping. Figure 6 shows the electrical resistivities as a function of temperature of a selection of samples normalized by the respective room temperature resistivity. All measured films showed a significant residual resistivity at low temperature, attributed to neutral impurity scattering. All measured films showed a continuous increase in resistivity above 110 K which implied the onset of deformation potential scattering. In the samples where the tin donors are deactivated, an increase in low temperature resistivity is observed, and such an effect could be attributed to ionized impurity scattering or weak localization [66, 67]. All films showed a similar increase in resistivity from 110 K to room temperature. Deformation potential-based scattering and neutral impurity

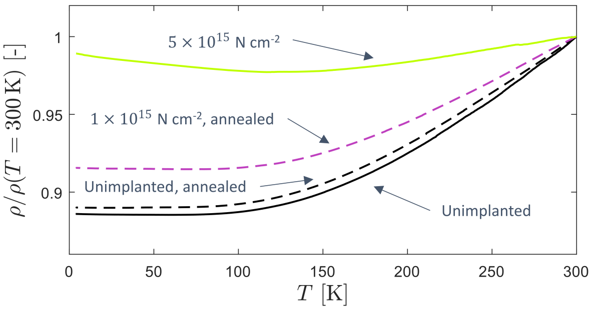

FIG. 6. (Color online) Temperature dependent sample resistivities normalized to their room temperature values.

scattering each contribute approximately 10 % and 90 % of the films' resistivity near room temperature, respectively. Therefore, the scattering parameter is assumed to be a weighted average of the contributing scattering mechanisms: $r = -0.05$. Historically, the scattering parameter in the non-parabolic band model for heavily degenerated ITO has been noted to fit experimental observation for values of r ranging between $r = -0.5$ by Ellmer and Meintus [68]. Guilmeau *et al.* [69] found that a weighted averaging of ionized impurity scattering and neutral impurity scattering leading to a fitted $r = 0.5 - 0.56$ was the best fit to experimental result with an assumed carrier effective mass of $m^* = 0.3m_0$ in the case of ITO as a heavily degenerated semiconductor. In summary, the effects of the $\mathrm{N_O}$ defect were evidenced through electrical and thermoelectric measurements, and the dominant room temperature scattering remained unchanged by the implantation, and important prerequisite for modelling through the Boltzmann transport model with the non-parabolic band approximation.

VI. DISCUSSION

Nitrogen implantation in ITO leads to the introduction of $\mathrm{N_O}^-$ acceptor states, resulting in a compensation of free carriers proportional to the implantation fluence. This effect was identified through high resolution core level XPS measurement shown in Figure 4(b) and through the increase in resistivity summarized in Table I. The relationship between carrier concentration and implantation fluence implied that the $\sim 4 \times 10^{20}\,\mathrm{cm^{-3}}$ electrons derived from the tin donors were deactivated by the $5 \times 10^{14}\,\mathrm{N\,cm^{-2}}$ implantation fluence. In addition, the magnitude of the Seebeck coefficient increased continuously in the implanted samples as the carrier concentrations reduced. The combined variation of these two intrinsic material properties allows for the carrier concentration-dependent effective mass to be evaluated. The quasi-linear Kane model for a conduction band defines band dispersion through

$$E(k) + CE(k)^2 = \frac{\hbar^2 k^2}{2m_0^*} \qquad (4)$$

where m_0^* is the effective mass at the conduction band edge, C is the first-order non-parabolicity factor, $\hbar$ is the reduced Planck's constant, k is the wavenumber, m_0^* is the band edge effective mass, and $E(k)$ is the energy [14]. By this formalism, the carrier concentration dependent effective mass can be written in terms of the carrier concentration as

$$m^* = m_0^* \sqrt{1 + 2C\frac{\hbar^2}{m_0^*}\left(3\pi^2 n\right)^{2/3}} \qquad (5)$$

in which n is the carrier concentration. To determine the carrier concentration dependent effective mass with Eq. 5, m_0^* and C must be determined from fitting the Seebeck coefficient and carrier concentration to experimental results. To do this within the power law relaxation time approximation, energies are rescaled by the unitless reduced energy given by $\tilde{E} = E/k_BT$. Similarly, the reduced Fermi energy is $\tilde{E}_F = E_F/k_BT$. For this calculation, the energy scale is taken relative to the conduction band edge. Assuming a spherically-symmetric density of states from the free-electron like conduction band with the quasi-linear Kane dispersion (Eq. 4), the carrier concentration can be calculated to be written as

$$n = \frac{1}{2\pi^2}\left(\frac{2m_0^* k_B T}{\hbar^2}\right)^{3/2} \times \int_0^{+\infty} \frac{\sqrt{\tilde{E}\left(1 + C\tilde{E}k_BT\right)}\left(1 + 2C\tilde{E}k_BT\right)}{e^{\tilde{E}-\tilde{E}_F} + 1}\,\mathrm{d}\tilde{E}. \qquad (6)$$

From the Boltzmann transport equations with the power law relaxation time approximation, the Seebeck coefficient can be expressed as

$$\alpha = \frac{k_B}{q}\left[\frac{\mathcal{F}^{\mathrm{NP}}_{r+\frac{3}{2}}}{\mathcal{F}^{\mathrm{NP}}_{r+\frac{1}{2}}} - \tilde{E}_F\right] \qquad (7)$$

in which a modified version of the Fermi integral is used, written

$$\mathcal{F}^{\mathrm{NP}}_s = \int_0^{+\infty}\left[(s+1) + \frac{1}{2}\frac{C\tilde{E}k_BT}{1 + C\tilde{E}k_BT}\right] \times \frac{\tilde{E}^s\sqrt{1 + C\tilde{E}k_BT}}{e^{\tilde{E}-\tilde{E}_F} + 1}\,\mathrm{d}\tilde{E}. \qquad (8)$$

in which $r = -0.05$ is used in this work as the scattering parameter, which determines the energy dependence of carrier lifetimes as by Eq. 3. All expressions (Eqs. 6, 7, 8) reduce to their usual forms in the condition $C = 0\,\mathrm{eV^{-1}}$, i.e., the parabolic band approximation. We plot $|n|$ and α from Table I as Figure 7, and draw the best-fitted non-parabolic and parabolic band Seebeck coefficient and carrier density relationships between those measured parameters at room temperature. For the fitting procedure we assume an exclusively diffusive Seebeck effect at room temperature in our films, evidenced by a linear dependence of the Seebeck coefficient with temperature as previously measured by Wu *et al.* [70] on similarly degenerately doped ITO samples.

The resulting best fit for our data on the Seebeck coefficient against carrier concentration plot is achieved the non-parabolic band with parameters $m_0^* = 0.21\,\mathrm{m_0}$ and $C = 0.52\,\mathrm{eV^{-1}}$. In the context of literature, historical Seebeck and Hall effect measurement approaches led to values of $0.14\,\mathrm{m_0}$ [7], $0.3\,\mathrm{m_0}$ [11], and $0.55\,\mathrm{m_0}$ [8]. Results from optical methods are $0.18\,\mathrm{m_0}$ [14], $0.22\,\mathrm{m_0}$ [12],

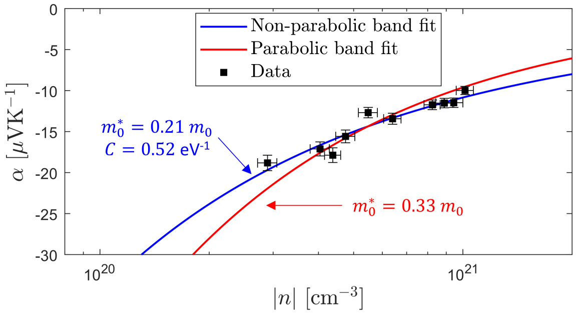

FIG. 7. (Color online) Seebeck coefficient and carrier concentration plot of data and best-fitting non-parabolic (red, $m_0^* = 0.21\,\mathrm{m}_0$ and $C = 0.52\,\mathrm{eV}^{-1}$) and parabolic (blue, $m_0^* = 0.33\,\mathrm{m}_0$) fits of Eqs. 6 and 7, both using $r = -0.05$.

$0.3\,\mathrm{m}_0$ [13, 71], and up to $0.5\,\mathrm{m}_0$ [72], which is also a rather large spread of results. It is possible that the non-parabolicity of the conduction band is the cause of the historical variation of measured effective masses of indium oxide and indium tin oxide, especially for highly doped samples. On the other hand, angle-resolved photoemission spectroscopy (ARPES) measurements have found band edge effective masses $0.22\,\mathrm{m}_0$ [73] and $0.21\,\mathrm{m}_0$ [74], with which our non-parabolic band edge fitting corroborates. If a scattering parameter $r = 0$ is used, the predicted band edge effective mass and first-order band non-parabolicity do not vary by more than $0.01\,\mathrm{m}_0$ and $0.01\,\mathrm{eV}^{-1}$, however, if r is further varied the resulting best-fitting m_0^* and C values become unphysical.

When the parabolic band condition ($C = 0\,\mathrm{eV}^{-1}$) is enforced, the best-fitting carrier effective mass was found to be $m_0^* = 0.33\,\mathrm{m}_0$. The best-fitting parabolic band model is in good agreement with the investigation of the effective mass of $0.30 \pm 0.03\,\mathrm{m}_0$ by Preissler *et al.* [11]. Over the fabricated range of carrier concentrations within the work between $2.9 \times 10^{20} \pm 0.2 \times 10^{20}\,\mathrm{cm}^{-3}$ and $10.1 \pm 0.6 \times 10^{20}\,\mathrm{cm}^{-3}$ the calculated effective mass varies between $0.33\,\mathrm{m}_0$ and $0.44\,\mathrm{m}_0$. The non-parabolicity of the conduction band is clearly an important feature of the overall carrier transport of ITO. Interestingly, the carrier mobility did not see an overall increase after annealing beyond $40\,\mathrm{cm}^2\mathrm{V}^{-1}\mathrm{s}^{-1}$ by the reduction in effective mass. This implies that the implanted nitrogen also contributes as a point defect scattering site, further supported by the increased residual resistivity proportion in the most-implanted film in Figure 6.

The band non-parabolicity determined in this work is compared to the band non-parabolicities determined from optical methods involving the plasma frequency by Liu *et al.* [4], Fujiwara and Kondo [13], and Feneberg *et al.* [14] in Figure 8(a). It is worth noting that as the calculated band edge effective mass is highest in the work of Fujiwara and Kondo [13], its band non-parabolicity is lowest. In contrast, Feneberg *et al.* [14] determined the opposite relationship, i.e, a low band edge effective mass and high band non-parabolicity. Liu *et al.* [4] and the calculations of this work find intermediate values for the band edge effective mass and first-order non-parabolicity factor. The Seebeck and Hall effect method results are in good agreement when compared to the optical method by Liu *et al.* [4]. Figure 8(b) shows the non-parabolicity relationship in closer detail, and compares it to the non-parabolicities determined by the other authors [4, 13, 14]. The low band non-parabolicity of the work of Fujiwara and Kondo [13] show a large initial effective mass, but one which does not increase notably until very high doping concentrations [13]. The similar values of C in the other works (Liu *et al.* [4] and Feneberg *et al.* [14]) show similar m^* and n relationships as the resulting fit in our work, however, are slightly offset by the differing band edge effective masses.

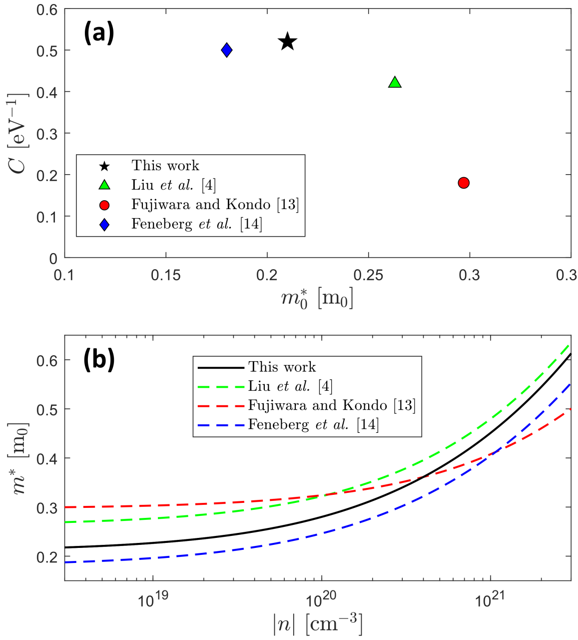

FIG. 8. (Color online) (a) How the band non-parabolicity factors found in references compared to the calculated combination of m_0^* and C in this work [4, 13, 14]. (b) Carrier effective mass in terms of carrier concentration for the non-parabolic band approximation calculated by Eq. 5 for the same referenced works.

We envisage that this type of approach of investigating the band non-parabolicity can be readily implemented on a range of degenerately doped conducting oxides, such as ZnO:Al or $\mathrm{SnO_2}$:F, and of course $\mathrm{In_2O_3}$:Sn. Excessive compensation of acceptor states by implantation may eventually irreversibly chemically modify the studied material, and is as such the reason that higher doping fluences should be avoided. The implantation fluences in future works must take into account the concentration of anion vacancies that are available to being filled by the compensating dopant. Further, structural relaxation by excessive implantation will eventually lead to the formation of separate phases, which would not possess the same transport character as the host semiconducting oxide.

Introducing acceptor state defects on donor vacancy sites is conceptually not limited to degenerate oxide thin film semiconductors. This would imply the applicability of this approach for a broader family of materials, where an acceptor with one lower atomic number could be used to substitute the anion in systems where the anion vacancy provides a high carrier concentration to the point of degeneracy. Since the method introduced by this work does not employ any optical measurements, a wider range of substrate choices are also possible, and the potential for measurements conducted on bulk samples is also possible. The band non-parabolicity in such materials can be investigated on films of materials which may require substrate material which conflicts with optical measurements, or bulk material where thin film growth provides particular challenge. The Seebeck and Hall effect method can provide vital information required for a wide range of practical applications such as thin film transistors, thermelectric generators, or solar cells due to the dependence of carrier transport on the electron effective mass which will affect the achievable carrier mobilities in such materials.

VII. CONCLUSION

The implantation of nitrogen in indium tin oxide thin films has been investigated, and the band non-parabolicity of ITO quantified by the quasi-linear Kane model through the Seebeck and Hall effect measurement method. We calculate a band non-parabolicity parameter of $C = 0.52\,\mathrm{eV}^{-1}$ and band edge effective mass $m_0^* = 0.21\,\mathrm{m}_0$, in good agreement with historical band edge photoemission, optical, and transport measurements. The presence of lattice-incorporated nitrogen in ITO was identified by XPS. The nitrogen implantation led to a notable reduction in the carrier concentration and carrier mobility. Theoretically, the $\mathrm{N_O}^-$ defect results in an electron localizing to the defect site, the free electron concentration reducing as a consequence. In addition, the band structure and projected density of states calculation implied that the localized deep acceptor $\mathrm{N_O}$ defect is situated above the valence band, and its electronic behavior is independent of neighboring tin atoms. This research opens the door for the application of the acceptor doping and the Seebeck and Hall effect approach with other anion vacancy driven n-type degenerate conducting thin films to investigate their band non-parabolicities.

CREDIT AUTHORSHIP CONTRIBUTION STATEMENT

Martin Markwitz: conceptualization, data curation, formal analysis, investigation, methodology, software, visualization, writing – original draft and editing. **Song Yi Back**: investigation, writing – review. **Edward X. M. Trewick**: investigation, writing – review. **Peter P. Murmu**: funding acquisition, writing – review. **Takao Mori**: funding acquisition, supervision, writing – review. **Ben J. Ruck**: funding acquisition, supervision, validation, writing – review. **John V. Kennedy**: funding acquisition, supervision, writing – review.

ACKNOWLEDGEMENTS

The authors would like to acknowledge Mr. Chris Purcell (National Isotope Centre, GNS Science, New Zealand) for conducting the RBS measurements. We acknowledge the surface analysis laboratory at UNSW in Australia for the XPS measurements. We acknowledge the helpful suggestions of Dr. Holger Fiedler (National Isotope Centre, GNS Science, New Zealand).

FUNDING

The authors acknowledge the Ministry of Business, Innovation and Employment, New Zealand (grant numbers C05X1802 and C05X1702) and JST Mirai Program, Japan (grant number JPMJMI19A1).

DECLARATION

The authors declare that they have no competing interests.

---

[1] S. Dixon, D. Scanlon, C. Carmalt, and I. Parkin, Journal of Materials Chemistry C **4**, 6946 (2016).
[2] J. Spencer, A. Mock, A. Jacobs, M. Schubert, Y. Zhang, and M. Tadjer, Applied Physics Reviews **9** (2022).
[3] P. Erhart, A. Klein, R. G. Egdell, and K. Albe, Physical Review B **75**, 153205 (2007).
[4] X. Liu, J. Park, J. Kang, H. Yuan, Y. Cui, H. Hwang, and M. Brongersma, Applied Physics Letters **105**, 181117 (2014).
[5] O. Bierwagen, Semiconductor Science and Technology **30**, 024001 (2015).
[6] O. Bierwagen and J. Speck, Physica Status Solidi (a) **211**, 48 (2014).
[7] J. De Wit, J. Van der Bom, and J. De Groot, Journal of Solid State Chemistry **25**, 101 (1978).
[8] R. Weiher, Journal of Applied Physics **33**, 2834 (1962).
[9] F. Fuchs and F. Bechstedt, Physical Review B **77**, 155107 (2008).

[10] Y. Shigesato, D. Paine, and T. Haynes, Journal of Applied Physics **73**, 3805 (1993).

[11] N. Preissler, O. Bierwagen, A. T. Ramu, and J. S. Speck, Physical Review B **88**, 085305 (2013).

[12] A. Vink, M. Overwijk, and W. Walrave, Journal of Applied Physics **80**, 3734 (1996).

[13] H. Fujiwara and M. Kondo, Physical Review B **71**, 075109 (2005).

[14] M. Feneberg, J. Nixdorf, C. Lidig, R. Goldhahn, Z. Galazka, O. Bierwagen, and J. S. Speck, Physical Review B **93**, 045203 (2016).

[15] Y. Shigesato and D. Haynes, Japanese Journal of Applied Physics **32**, L1352 (1993).

[16] T. Haynes, Y. Shigesato, I. Yasui, N. Taga, and H. Odaka, Nuclear Instruments and Methods in Physics Research Section B: Beam Interactions with Materials and Atoms **121**, 221 (1997).

[17] Z. Huang, H. Ruan, H. Zhang, D. Shi, W. Li, G. Qin, F. Wu, L. Fang, and C. Kong, Optical Materials Express **9**, 3098 (2019).

[18] R. Ramos, D. Scoca, R. Merlo, F. Marques, F. Alvarez, and L. Zagonel, Applied Surface Science **443**, 619 (2018).

[19] R. Sethi, P. Kumar, S. Khan, A. Aziz, and A. Siddiqui, in *AIP Conference Proceedings*, Vol. 1742 (AIP Publishing LLC, 2016) p. 030016.

[20] J. Biersack, S. Berg, and C. Nender, Nuclear Instruments and Methods in Physics Research Section B: Beam Interactions with Materials and Atoms **59**, 21 (1991).

[21] A. Markwitz and J. Kennedy, International Journal of Nanotechnology **6**, 369 (2009).

[22] H. Fiedler, P. Gupta, J. Kennedy, and A. Markwitz, Review of Scientific Instruments **89**, 123305 (2018).

[23] J. Kennedy, G. V. M. Williams, P. P. Murmu, and B. J. Ruck, Physical Review B **88**, 214423 (2013).

[24] J. Kennedy, A. Markwitz, H. Trodahl, B. Ruck, S. Durbin, and W. Gao, Journal of Electronic Materials **36**, 472 (2007).

[25] N. Fairley, V. Fernandez, M. Richard-Plouet, C. Guillot-Deudon, J. Walton, E. Smith, D. Flahaut, M. Greiner, M. Biesinger, S. Tougaard, *et al.*, Applied Surface Science Advances **5**, 100112 (2021).

[26] P. Hohenberg and W. Kohn, Physical Review **136**, B864 (1964).

[27] W. Kohn and L. Sham, Physical Review **140**, A1133 (1965).

[28] P. Giannozzi, O. Andreussi, T. Brumme, O. Bunau, M. Nardelli, M. Calandra, R. Car, C. Cavazzoni, D. Ceresoli, M. Cococcioni, *et al.*, Journal of Physics: Condensed Matter **29**, 465901 (2017).

[29] P. Giannozzi, O. Baseggio, P. Bonfà, D. Brunato, R. Car, I. Carnimeo, C. Cavazzoni, S. De Gironcoli, P. Delugas, F. Ferrari Ruffino, *et al.*, The Journal of Chemical Physics **152**, 154105 (2020).

[30] A. Dal Corso, Computational Materials Science **95**, 337 (2014).

[31] J. P. Perdew, K. Burke, and M. Ernzerhof, Physical Review Letters **77**, 3865 (1996).

[32] H. Monkhorst and J. Pack, Physical Review B **13**, 5188 (1976).

[33] P. V. C. Medeiros, S. Stafström, and J. Björk, Physical Review B **89**, 041407(R) (2014).

[34] P. V. C. Medeiros, S. S. Tsirkin, S. Stafström, and J. Björk, Physical Review B **91**, 041116(R) (2015).

[35] M. Iraola, J. Mañes, B. Bradlyn, M. Horton, T. Neupert, M. Vergniory, and S. Tsirkin, Computer Physics Communications **272**, 108226 (2022).

[36] L. Gupta, A. Mansingh, and P. K. Srivastava, Thin Solid Films **176**, 33 (1989).

[37] J. Lento, J. Mozos, and R. Nieminen, Journal of Physics: Condensed Matter **14**, 2637 (2002).

[38] S. Lany and A. Zunger, Physical Review B **78**, 235104 (2008).

[39] K. Irmscher, M. Naumann, M. Pietsch, Z. Galazka, R. Uecker, T. Schulz, R. Schewski, M. Albrecht, and R. Fornari, Physica Status Solidi (a) **211**, 54 (2014).

[40] S. Lany and A. Zunger, Physical Review Letters **98**, 045501 (2007).

[41] S. Lany and A. Zunger, Physical Review B **72**, 035215 (2005).

[42] C. Persson, Y. J. Zhao, S. Lany, and A. Zunger, Physical Review B **72**, 035211 (2005).

[43] S. Dudarev, G. Botton, S. Savrasov, C. Humphreys, and A. Sutton, Physical Review B **57**, 1505 (1998).

[44] P. Reunchan, N. Umezawa, A. Janotti, T. Jiraroj, and S. Limpijumnong, Physical Review B **95**, 205204 (2017).

[45] Z. G. Yu, J. Sun, M. B. Sullivan, Y. W. Zhang, H. Gong, and D. J. Singh, Chemical Physics Letters **621**, 141 (2015).

[46] I. Chatratin, F. P. Sabino, P. Reunchan, S. Limpijumnong, J. B. Varley, C. G. Van de Walle, and A. Janotti, Physical Review Materials **3**, 074604 (2019).

[47] J. E. Swallow, B. A. D. Williamson, S. Sathasivam, M. Birkett, T. J. Featherstone, P. A. E. Murgatroyd, H. J. Edwards, Z. W. Lebens-Higgins, D. A. Duncan, M. Farnworth, P. Warren, N. Peng, T. L. Lee, L. F. J. Piper, A. Regoutz, C. J. Carmalt, I. P. Parkin, V. R. Dhanak, D. O. Scanlon, and T. D. Veal, Materials Horizons **7**, 236 (2020).

[48] J. L. Lyons, A. Janotti, and C. G. Van de Walle, Applied Physics Letters **95** (2009).

[49] S. Lany and A. Zunger, Physical Review B **81**, 205209 (2010).

[50] K. Momma and F. Izumi, Journal of Applied Crystallography **41**, 653 (2008).

[51] K. Momma and F. Izumi, Journal of Applied Crystallography **44**, 1272 (2011).

[52] M. Markwitz, P. Murmu, S. Back, T. Mori, B. Ruck, and J. Kennedy, Surfaces and Interfaces **41**, 103190 (2023).

[53] P. Murmu, A. Shettigar, S. Chong, Z. Liu, D. Goodacre, V. Jovic, T. Mori, K. Smith, and J. Kennedy, Journal of Materiomics **7**, 612 (2021).

[54] W. Wu and B. Chiou, Semiconductor Science and Technology **11**, 196 (1996).

[55] S. Yang, C. Zhang, Z. Yang, J. Yao, H. Wang, and G. Ding, Journal of Alloys and Compounds **778**, 90 (2019).

[56] D. Maestre, A. Cremades, L. Gregoratti, and J. Piqueras, The Journal of Physical Chemistry C **114**, 3411 (2010).

[57] Z. Liu, J. Liang, H. Zhou, W. Lu, J. Li, B. Wang, Q. Li, X. Zhao, and J. Xu, Applied Surface Science **594**, 153508 (2022).

[58] Y. Ren, P. Liu, R. Liu, Y. Wang, Y. Wei, L. Jin, and G. Zhao, Journal of Alloys and Compounds **893**, 162304 (2022).

[59] M. Biesinger, Applied Surface Science **597**, 153681 (2022).

[60] L. Tian, G. Cheng, H. Wang, Y. Wu, R. Zheng, and P. Ding, Superlattices and Microstructures **101**, 261 (2017).

[61] M. Himmerlich, M. Koufaki, C. Mauder, G. Ecke, V. Cimalla, J. Schaefer, E. Aperathitis, and S. Krischok, Surface Science **601**, 4082 (2007).

[62] M. Himmerlich, M. Koufaki, G. Ecke, C. Mauder, V. Cimalla, J. Schaefer, A. Kondilis, N. Pelekanos, M. Modreanu, S. Krischok, and E. Aperathitis, ACS Applied Materials & Interfaces **1**, 1451 (2009).

[63] K. Reyes-Gil, E. Reyes-García, and D. Raftery, The Journal of Physical Chemistry C **111**, 14579 (2007).

[64] G. Greczynski and L. Hultman, Applied Surface Science **542**, 148599 (2021).

[65] M. Maaza, O. Nemraoui, A. Beye, C. Sella, and T. Derry, Solar Energy Materials and Solar Cells **90**, 111 (2006).

[66] D. Kaushik, K. Kumar, and A. Subrahmanyam, AIP Advances **7** (2017).

[67] M. Nistor, F. Gherendi, and J. Perrière, Materials Science in Semiconductor Processing **88**, 45 (2018).

[68] K. Ellmer and R. Mientus, Thin Solid Films **516**, 5829 (2008).

[69] E. Guilmeau, D. Bérardan, C. Simon, A. Maignan, B. Raveau, D. Ovono, and F. Delorme, Journal of Applied Physics **106**, 053715 (2009).

[70] C. Y. Wu, T. V. Thanh, Y. F. Chen, J. K. Lee, and J. J. Lin, Journal of Applied Physics **108** (2010).

[71] H. K. Müller, Physica Status Solidi (b) **27**, 733 (1968).

[72] V. M. Vainshtein and V. I. Fistul, Sov. Phys. Semiconductors **4**, 1278 (1971).

[73] K. H. L. Zhang, R. G. Egdell, F. Offi, S. Iacobucci, L. Petaccia, S. Gorovikov, and P. D. C. King, Physical Review Letters **110**, 056803 (2013).

[74] V. Scherer, C. Janowitz, A. Krapf, H. Dwelk, D. Braun, and R. Manzke, Applied Physics Letters **100** (2012).